CARDIFF UNIVERSITY
PRIFYSGOL CAERDYDD

ORCA – Online Research @ Cardiff

This is an Open Access document downloaded from ORCA, Cardiff University's institutional repository:https://orca.cardiff.ac.uk/id/eprint/136174/

This is the author's version of a work that was submitted to / accepted for publication.

Citation for final published version:

Starr, Aidan, Hall, Ian R. , Barker, Stephen , Rackow, Thomas, Zhang, Xu, Hemming, Sidney R., van der Lubbe, H. J. L., Knorr, Gregor, Berke, Melissa A., Bigg, Grant R., Cartagena, Alejandra, Jiménez-Espejo, Francisco, Gong, Xun, Gruetzner, Jens, Lathika, Nambiyathodi, LeVay, Leah J., Robinson, Rebecca S., Ziegler, Martin and Exp. 361 Science Party 2021. Antarctic icebergs reorganise ocean circulation during pleistocene glacials. Nature 589 , pp. 236-241. 10.1038/s41586-020-03094-7

Publishers page: http://dx.doi.org/10.1038/s41586-020-03094-7

Please note:
Changes made as a result of publishing processes such as copy-editing, formatting and page numbers may not be reflected in this version. For the definitive version of this publication, please refer to the published source. You are advised to consult the publisher's version if you wish to cite this paper.

This version is being made available in accordance with publisher policies. See http://orca.cf.ac.uk/policies.html for usage policies. Copyright and moral rights for publications made available in ORCA are retained by the copyright holders.

Antarctic Icebergs Reorganize Ocean Circulation During Pleistocene Glacials

Aidan Starr[1], Ian R. Hall[1], Stephen Barker[1], Thomas Rackow[2], Xu Zhang[3,4], Sidney R. Hemming[5], H.J.L van der Lubbe[1,6], Gregor Knorr[2], Melissa A. Berke[7], Grant R. Bigg[8], Alejandra Cartagena[7], Francisco J. Jiménez-Espejo[9,10], Xun Gong[2,11], Jens Gruetzner[2], Nambiyathodi Lathika[12], Leah J. LeVay[13], Rebecca S. Robinson[14], Martin Ziegler[15], and Exp. 361 Science Party

[1]School of Earth and Environmental Sciences, Cardiff University, Cardiff, UK
[2]Alfred-Wegener-Institute, Helmholtz Centre for Polar and Marine Science, Bremerhaven, DE
[3]Center for Pan Third Pole Environment (Pan-TPE), Key Laboratory of Western China's Environmental Systems (Ministry of Education), College of Earth and Environmental Science, Lanzhou University, Lanzhou, CN
[4]CAS Center for Excellence in Tibetan Plateau Earth Sciences, Chinese Academy of Sciences (CAS), Beijing, CN
[5]Department of Earth and Environmental Sciences and Lamont-Doherty Earth Observatory of Columbia University, Palisades, New York, USA
[6]Faculty of Science, Vrije University, Amsterdam, NL
[7]Department of Civil & Environmental Engineering and Earth Sciences, University of Notre Dame, Indiana, USA
[8]Department of Geography, University of Sheffield, Sheffield, UK
[9]Instituto Andaluz de Ciencias de la Tierra (CSIC-UGR), Armilla, ES
[10]Department of Biogeochemistry, JAMSTEC, Yokosuka, JP
[11]Hubei Key Laboratory of Marine Geological Resources, China University of Geosciences, Wuhan, CN
[12]National Centre for Polar and Ocean Research, Goa, IN
[13]International Ocean Discovery Program, Texas A& M University, College Station, Texas, USA
[14]Graduate School of Oceanography, University of Rhode Island, Narragansett, Rhode Island, USA
[15]Department of Earth Sciences, Utrecht University, Utrecht, NL

The dominant feature of large-scale mass transfer in the modern ocean is the Atlantic meridional overturning circulation (AMOC). The geometry and vigour of this circulation influences global climate on various timescales. Paleoceanographic evidence suggests that during glacial periods of the past 1.5 million years the AMOC was markedly different from modern[1]: in the Atlantic basin, deep waters of Southern Ocean origin increased in volume whilst above them the core of the North Atlantic Deep Water (NADW) shoaled[2]. An absence of evidence to elucidate the origin of this phenomenon means that the sequence of events during the descent into global glacial conditions remains unclear. Here, we present multi-proxy evidence showing that northward shifts in Antarctic iceberg melt in the Indian-Atlantic Southern Ocean systematically preceded deep-water mass reorganisations by 1-2 thousand-years (kyr) during Pleistocene glaciations. With the aid of new iceberg trajectory model experiments, we demonstrate such a shift in iceberg trajectories during glacial periods can result in a considerable redistribution of freshwater in the Southern Ocean. We suggest that this, in concert with increased sea-ice cover, allowed positive buoyancy anomalies to 'escape' into the upper limb of the AMOC, providing a teleconnection between surface Southern Ocean conditions and the formation of NADW. The magnitude and pacing of this mechanism evolved substantially across the Mid-Pleistocene Transition (MPT), and the coeval increase in magnitude of the 'southern escape' and deep circulation perturbations implicate this mechanism as a key feedback in the transition to the 100-kyr world.

In the modern ocean, the AMOC is characterised by the deep, southward spread of NADW towards the Southern Ocean (SO), balanced by the northward return of surface, mode, intermediate, and bottom

waters[3,4]. Whilst the widely documented shoaling of NADW during Pleistocene glacial periods has previously been explained through changes in North Atlantic processes[5], this paradigm has been challenged by studies invoking 'upstream' disruptions (e.g. variable Agulhas Leakage[6,7]), modifying the shallow return of waters to the North Atlantic required to complete this 'Upper Cell' of the overturning circulation. Furthermore, the southward and northward components of the Upper Cell are connected via wind- and buoyancy-related processes in the SO, with much of the outcropping NADW first taking an indirect route, via the so-called 'Lower Cell' of overturning circulation, before joining the AMOC return limb via the upper cell[4] (Extended Data Figure 1). SO conditions have therefore been increasingly invoked by modelling studies[7–9] as key in setting NADW dynamics, however paleoceanographic evidence supporting such a causal link remains scarce[10].

Here we show a tight surface-deep coupling between the presence of far-travelled Antarctic icebergs and deep-water mass structure at the northern limit of the modern Subantarctic Zone (SAZ) during the past 1.65 Million Years (Ma). We examine new and previously published records of ice-rafted debris mass accumulation rate[11,12] (IRD_{MAR}), and carbon and oxygen isotope records[13] from benthic foraminifera ($\delta^{13}C_{benthic}$, $\delta^{18}O_{benthic}$) from a new composite record of sediment cores recovered from the Agulhas Plateau in the south-west Indian Ocean. Spanning the past 1.65 Ma, the 'Agulhas Plateau Composite' (hereafter the AP_{comp}; see online methods for age model and composite construction) consists of MD02-2588 (41°19.90'S, 25°49.70'E, 2907 m water depth) and International Ocean Discovery Program (IODP) Site U1475 (41°25.60'S, 25°15.60'E, 2669 m water depth).

Iceberg Trajectories and Deep Hydrography

The Agulhas Plateau is situated at the southern boundary of the Indian-Atlantic Ocean Gateway (Figure 1a); the upper water column is dominated by eastward flowing Indian Ocean surface waters retroflected as the Agulhas Return Current (i.e. not 'leaked' into the South Atlantic). To the south, the relatively cold and fresh waters of the SAZ meet their northern limit, forming steep hydrographic gradients at the subtropical frontal zone (STFZ; Figure 1). Iceberg presence (and subsequently IRD deposition) at this location can therefore be influenced by regional hydrography (i.e shifts in the STFZ) as well as the export, survivability, and transport of icebergs into and across the SO. To aid in our interpretation of the IRD_{MAR} proxy, we perform iceberg trajectory modelling experiments using Pyberg, an offline implementation of the Finite Element Sea Ice-Ocean Model (FESOM-IB)[14] iceberg drift and decay module. We force Pyberg with the Community Earth System Models (COSMOS)[15] run to quasi-equilibrium under Pre-Industrial (PI) and Last Glacial Maximum (LGM) climate conditions (see online methods). In each experiment, 111 icebergs were seeded from observationally-derived locations in the Weddell Sea 'iceberg alley' (online methods; shaded box in Figure 1a) and are treated as passive particles, moving and decaying according to oceanic (including sea-ice) and atmospheric conditions. In reality the mass balance and discharge of icebergs from the Antarctic Ice Sheet was likely variable in the past, however by initializing these experiments with consistent iceberg seeding, and neglecting a possible Subantarctic source of icebergs[16] (on the petrological grounds outlined in the online methods), we are able to assess the relative redistribution of iceberg melt resulting only from changes in SO conditions.

Much as the surface hydrography at the Agulhas Plateau represents a junction between subantarctic and subtropical regimes, the deep circulation is characterised by competing Northern- and Southern-sourced water masses (NSW and SSW, respectively). NSW here refers to NADW, and glacial analogues, which today extends to 3000m water depth as it exits the Atlantic Ocean into the SO[3]. A weakening and shoaling of NSW, as in some glacial reconstructions[2], would result in increased presence of SSW at the Agulhas Plateau, consisting of some combination of Lower Circumpolar Deep Water and Antarctic Bottom Water, flowing clockwise around the SO, and spreading northwards into the neighbouring subtropical basins[4]. We examine the relative contribution of NSW vs SSW at the Agulhas Plateau through

the $\delta^{13}C$ of Cibicidoides wuellerstorfi, an epifaunal benthic foraminifer shown previously to be closely related to the $\delta^{13}C_{DIC}$ of ambient seawater[17], and therefore a widely applied proxy to trace past changes in deep ocean ventilation by ocean circulation[1,2].

As with the IRD proxy, the $\delta^{13}C_{benthic}$ record may be influenced by numerous environmental processes. In other words, it is not a simple water mass tracer, and may be affected additionally by productivity signals[18] and non-stationary water mass end-members[19]. After accounting for time-varying end-member signatures using a binary mixing model (Extended Data Figure 4) we find that the %NSW is well correlated to the raw $\delta^{13}C_{benthic}$ record at the AP_{comp} (r^2=0.39), supporting our interpretation that relative NSW versus SSW presence at the site is the dominant control on $\delta^{13}C_{benthic}$. This inference is in agreement with complementary water mass tracers[20] and basin-wide data compilations and modelling studies[2]. The timing of $\delta^{13}C_{benthic}$ changes recorded in the AP_{comp} can therefore be instructive in identifying the origin of deep circulation changes with respect to surface SO conditions recorded in the co-registered IRD_{MAR} data.

Surface-Deep Phasing

The glacial AP_{comp} is characterised by generally higher IRD_{MAR} and lower $\delta^{13}C_{benthic}$ (shaded bars in Figure 2) compared to interglacials, reflecting the increased presence of Antarctic icebergs and the reduced presence of NSW, respectively. A significant negative correlation is present between IRD_{MAR} and $\delta^{13}C_{benthic}$ (r^2 = -0.39), becoming stronger still when IRD_{MAR} is log-transformed (r^2 = -0.54). The reason for log-transforming the IRD_{MAR} data is twofold: firstly, it has a strongly skewed distribution with a small number of very high values. Secondly, we consider log-IRD_{MAR} a more sensitive indicator of paleo-iceberg drift, for example the probability of iceberg presence in the SO decreases by orders of magnitude with distance north of the main iceberg belt in the Weddell Sea sector[21]. To explore the phasing of the close relationship between the co-registered surface and deep AP_{comp} conditions we employ three independent approaches. The strongest correlation between the two records (r^2 = -0.59) occurs when IRD_{MAR} leads $\delta^{13}C_{benthic}$ by 2±1 kyrs (Extended Data Figure 5d), and spectral coherency analysis reveals a lead for IRD_{MAR} in all three major Milankovitch frequency bands (Figure 3a). Additionally, a numerical algorithm which determines the offsets between peaks in rate of change reveals that maxima in the IRD_{MAR} occur on average 1.65±0.59 kyrs before maxima in the rate of $\delta^{13}C_{benthic}$ decrease (Figure 3b). Together, these approaches independently demonstrate that IRD_{MAR} systematically leads $\delta^{13}C_{benthic}$ at the AP_{comp}; the unidirectional result from the 'peak lag algorithm' best allows us to quantify this lead as 1-2 kyrs, providing a valuable constraint on the link between the SO surface variability and deep water-mass geometry during transitions from interglacial to glacial conditions over the past 1.65 Ma.

Understanding this relationship further requires a robust interpretation of both the IRD_{MAR} and $\delta^{13}C_{benthic}$ proxies. For example, we might interpet higher glacial IRD_{MAR} as indicating a glacial shift in iceberg trajectories. This interpretation is coherent with published IRD records which show that deposition close to Antarctica is generally highest during interglacial periods[22,23] and periods of ice sheet retreat[23,24] (e.g. glacial terminations), whilst at SAZ locations IRD maxima typically occur during glacial periods (this study;[22,25]). From this we can deduce that glacial conditions in the SO favour the increased transport of icebergs away from Antarctica (Figure 1), as the early decay of icebergs is reduced and the overall survivability and transport enhanced, due to cooler surface temperatures[26], increased sea-ice[26,27], and changes in surface circulation, possibly relating to the westerly-wind belt. Iceberg drift in the ocean is associated with, and can facilitate sea-ice formation[21], and sea-ice presence in turn can inhibit the wave-driven erosion of icebergs[28] and govern iceberg movement under severe ice conditions[29]. Enhanced sea-ice concentration and extent is a well-documented feature of the glacial SO[26], and the close correspondence between the AP_{comp} IRD_{MAR} record and an Antarctic ice core proxy for sea ice extent[27] (Figure 2) over the past 8 glacial cycles suggests that such a feedback may be important.

Furthermore, our modelling results indicate that LGM conditions are associated with an equatorward shift and lengthening of trajectories relative to PI (Figure 1) and modern observations[30]. Whilst long-term IRD_{MAR} variability in the SAZ is likely influenced by varied calving rates, a dramatically altered distribution of icebergs does not require a substantial change to ice sheet mass balance. We acknowledge, however, that iceberg presence and therefore IRD deposition at the AP_{comp} does require some calving of icebergs to occur, and therefore necessitates a sufficiently large ice sheet. Considering evidence that East Antarctica maintained a marine-terminating ice sheet across the warm interglacial Marine Isotope stage (MIS) 31[31], we reason that the calving-ice-sheet-condition would have been consistently met during the glacial intervals relevant to our proposed mechanism[32].

The Southern Escape

In the modern ocean the conveyor of icebergs traversing the SO constitutes a major transport of meteoric freshwater away from the Antarctic Ice Sheet, particularly in the Weddell Sea sector[33]: a sizeable fraction of modern iceberg mass (up to 35% for giant icebergs[14,33]) can be exported north of 63°S. By estimating iceberg meltwater inputs from our trajectory experiments (online methods), we find a substantial redistribution of freshwater in the SO, as the latitude at which this meltwater is greatest shifts several degrees to the north under glacial conditions, with meltwater input south of 50°S diminishing (Figure 1). Furthermore, we find nearly twice as much meltwater in the region between 0-50°E under LGM conditions compared to PI conditions (22.7% and 40.7%, respectively, of the total initial iceberg mass (online methods)). Whilst this is clearly an idealized representation, with no change in calving-rate imposed between experiments, it demonstrates that changes in SO conditions can dramatically alter the buoyancy budget of the SO. For example in the modern SO, the meltwater associated with iceberg maxima can exceed the local precipitation-evaporation balance[14].

A connection between SO surface forcing and the deep ocean has been explored through a variety of theoretical lenses. A common theme occurs wherein enhanced sea-ice (formation and extent) results in an expansion of the region of net surface buoyancy loss[8,9], due to increased brine rejection close to, and subsequent melt occurring away from, the continent. However, the ability of sea-ice buoyancy forcing alone to explain the full NSW shoaling implied by paleoceanographic evidence has been questioned[34] and such a direct link is challenged by the failure of climate models without additional cooling in the SO[15] to simulate a shoaled glacial NSW. We suggest that the equatorward shift in Antarctic iceberg melt, a feature absent from the aforementioned models, may be a key, previously unconsidered component in connecting the surface SO to overturning circulation. This would allow positive buoyancy anomalies to effectively 'escape' the SO into the return AMOC limb; ultimately influencing deepwater formation in the Upper (NSW) instead of the Lower (SSW) overturning cell. The return limb of AMOC consists of surface to intermediate waters entering the South Atlantic gyre[4] through northward Ekman transport across the SO and entrainment in South Atlantic Subtropical Gyre, or via the shedding of warm and saline mesoscale eddies by the so-called Agulhas Leakage[35] (Figure 1a). The importance of this return limb is illustrated by the role of Agulhas Leakage in the resumption of NADW formation at glacial terminations, when an increase in the inter-ocean exchange of salt transfers positive density anomalies into the Atlantic basin, triggering the resumption of a strong, deep AMOC mode[7,36]. The corollary would suggest that reducing the density export into the South Atlantic, for example through the 'southern escape' of iceberg meltwater, would have the inverse effect: suppressing NADW formation.

Such a mechanism finds support from SO 'hosing' experiments which find that freshwater addition in the SO (in these experiments, south of 60°S) can affect NADW formation[37,38] due to Ekman spread of surface waters away from the SO. However, these experiments also generate a weaker Lower Cell: the paleoceanographic evidence for which remains equivocal. Whilst sea-ice formation may have stimulated the Lower Cell[39], grounded ice cover in coastal regions of AABW formation may have an opposing

effect[32,40]. At the Agulhas Plateau, negative $\delta^{13}C_{benthic}$ excursions during glacial periods of the past 200 ka are associated with increased near-bottom flow speeds[41], indicating a vigorous yet poorly-ventilated glacial SSW (i.e. lower overturning cell) consistent with increased AABW convection[10] fed by surface waters isolated from the atmosphere by enhanced sea-ice[39]. That being said, the 1-2 kyr lag time observed here is difficult to reconcile with a direct SO mechanism and the temporal offset between IRD_{MAR} and $\delta^{13}C_{benthic}$ may instead favour a teleconnection operating with a threshold behaviour. For example, while the northward export of icebergs to the SAZ would directly decrease the buoyancy flux in AABW formation regions, NADW formation may initially remain strong enough to prevent the northward/upward expansion of SSW. This would continue until the associated 'escape' of buoyancy anomalies into the Upper Cell has gradually weakened NADW formation across some threshold whereby the expansion of SSW into the deep Atlantic is possible.

Orbital Pacing and Sequence of Events

With this mechanism in mind, we next examine the timing of events at the AP_{comp} in the context of global climate. In agreement with evidence for an early climate signal in the SO during interglacial-glacial transitions[10,42,43] we find that IRD_{MAR} leads $\delta^{18}O_{benthic}$ at all three significant orbital frequency bands (Figure 3a). Under the assumption that $\delta^{18}O_{benthic}$ changes synchronously with global climate, this would imply that IRD_{MAR} peaks lead relative to global climate (or at least Northern Hemisphere ice volume). Moreover, a distinct inter-hemispheric asynchrony is suggested by the phasing of IRD between the SO and the North Atlantic: IRD peaks at the AP_{comp} typically precede IRD peaks at ODP Site 982[44] (Figure 4d). A sequence of events emerges in which at the onset of glacial periods a northward expansion of Antarctic iceberg melt occurs, facilitated by increased sea ice extent and surface cooling in the SO[10], preceding the descent into full global glacial conditions as indicated by maxima in the global $\delta^{18}O_{benthic}$ record. The external forcing of this sequence of events may therefore be identified by the external forcing of SST and sea-ice in the SO; a role for which obliquity has been invoked[45]. Indeed, we observe cooler surface conditions in our low obliquity model experiment (LGM27ka), compared to LGM (Extended Data 6) and find that icebergs travel further and decay more slowly between 'iceberg alley' and the Atlantic-Indian SAZ. This is consistent with existing SST reconstructions from the Agulhas Plateau[46] showing colder SST during lower obliquity (Figure 2b).

The pacing of IRD_{MAR} peaks by obliquity is apparent during cycles before ~1.2 Ma (MIS 36) and after ~0.4 Ma (MIS 11; Figure 4b), however is somewhat obscured inbetween during the Mid-Pleistocene Transition (MPT). During the MPT, the dominant cyclicity in IRD_{MAR} shifts from ~ 40-kyr^{-1} to ~ 100-kyr^{-1}, possibly reflecting a transition to a nonlinear response to orbital forcing associated with larger ice-sheets[47]. We note that the surface-deep lead (IRD_{MAR} versus $\delta^{13}C_{benthic}$) is relatively constant at 1-2 kyr for the entire 1.65 Ma record, however the lead of SO processes over maxima in $\delta^{18}O_{benthic}$ (and hence glacial conditions) is variable, increasing between ~1.2 Ma and ~0.4 Ma. For example, during MIS 24-26, >80% of the total IRD_{MAR} accumulated within the first 50% of the glacial cycle (Figure 4a). This is compared to ~60% accumulation by halfway through the pre- and post-MPT cycles. An increase in this lead of SO processes over global ice volume may have resulted from growing larger ice sheets across the MPT (which would take longer to develop), with the return to a shorter lead time in the Late Pleistocene implying that the rate of ice sheet growth had increased to accommodate this larger size. Interestingly, recent evidence from the North Atlantic suggests that the rate of northern ice sheet growth may have accelerated across the MPT, reaching a maximum after ~0.6 Ma, as a consequence of increasing Atlantic Inflow into the Nordic Seas since ~1.2 Ma (SB, GK, XZ, et al., *submitted*). Furthermore, glacial IRD_{MAR} maxima at the AP_{comp} increase across the MPT (Figure 4d), beginning at MIS 36 (~1.2 Ma) and likely reflecting enhanced export of icebergs across the SAZ, coincident with surface cooling and freshening in the Atlantic SO[48].

While this long-term trend may be driven by increasingly iceberg-favourable (cooler) conditions in the region[48], we cannot rule out a role for some change in the discharge of Antarctic icebergs amid a background of global cooling and possible transitions in the character of Antarctic ice sheets[49]. Regardless, the southern escape of freshwater (IRD_{MAR}) into the SAZ appears to scale with the magnitude of glacial AMOC perturbations as indicated by $\delta^{13}C_{benthic}$ minima; notably, the IRD_{MAR} maximum (and $\delta^{13}C_{benthic}$ minimum) at ~0.9 Ma coincides with the implied collapse in AMOC as recorded in the nearby deep Cape Basin[50]. This apparent scaling, as well as the consistent temporal coupling between the southern escape of freshwater and deep water-mass perturbations across this interval, implicate this feedback as a central ingredient in setting overturning circulation state across the MPT and in doing so, perhaps promoting the sequestration of atmospheric CO_2 during the longer glacial intervals of the 100-kyr world[19].

References

1. Lisiecki, L. E. Atlantic overturning responses to obliquity and precession over the last 3 Myr. *Paleoceanography* **29,** 71–86 (2014).
2. Hesse, T., Butzin, M., Bickert, T. & Lohmann, G. A model-data comparison of δ13C in the glacial Atlantic Ocean. *Paleoceanography* **26** (2011).
3. Bower, A. *et al.* Lagrangian Views of the Pathways of the Atlantic Meridional Overturning Circulation. *Journal of Geophysical Research: Oceans* **124,** 5313–5335 (2019).
4. Talley, L. D. Closure of the global overturning circulation through the Indian, Pacific, and southern oceans. *Oceanography* **26,** 80–97 (2013).
5. Swingedouw, D., Braconnot, P., Delecluse, P., Guilyardi, E. & Marti, O. The impact of global freshwater forcing on the thermohaline circulation: Adjustment of North Atlantic convection sites in a CGCM. *Climate Dynamics* **28,** 291–305 (2007).
6. Caley, T., Giraudeau, J., Malaizé, B., Rossignol, L. & Pierre, C. Agulhas leakage as a key process in the modes of Quaternary climate changes. *Proceedings of the National Academy of Sciences of the United States of America* **109,** 6835–6839 (2012).
7. Knorr, G. & Lohmann, G. Southern ocean origin for the resumption of Atlantic thermohaline circulation during deglaciation. *Nature* **424,** 532–536 (2003).
8. Watson, A. J., Vallis, G. K. & Nikurashin, M. Southern Ocean buoyancy forcing of ocean ventilation and glacial atmospheric CO2. *Nature Geoscience* **8,** 861–864 (2015).
9. Ferrari, R. *et al.* Antarctic sea ice control on ocean circulation in present and glacial climates. *Proceedings of the National Academy of Sciences of the United States of America* **111,** 8753–8758 (2014).
10. Govin, A. *et al.* Evidence for northward expansion of Antarctic Bottom Water mass in the Southern Ocean during the last glacial inception. *Paleoceanography* **24,** 1–14 (2009).
11. Marino, G. *et al.* Agulhas salt-leakage oscillations during abrupt climate changes of the Late Pleistocene. *Paleoceanography* **28,** 599–606 (2013).
12. Simon, M. H. *et al.* Millennial-scale Agulhas Current variability and its implications for salt-leakage through the Indian-Atlantic Ocean Gateway. *Earth and Planetary Science Letters* **383,** 101–112 (2013).
13. Ziegler, M., Diz, P., Hall, I. R. & Zahn, R. Millennial-scale changes in atmospheric CO2 levels linked to the Southern Ocean carbon isotope gradient and dust flux. *Nature Geoscience* **6,** 457–461 (2013).
14. Rackow, T. *et al.* A simulation of small to giant Antarctic iceberg evolution: Differential impact on climatology estimates. *Journal of Geophysical Research: Oceans* **122,** 3170–3190 (2017).

15. Zhang, X., Lohmann, G., Knorr, G. & Xu, X. Different ocean states and transient characteristics in last glacial maximum simulations and implications for deglaciation. *Climate of the Past* **9,** 2319–2333 (2013).

16. Bigg, G. R. The impact of icebergs of sub-Antarctic origin on Southern Ocean ice-rafted debris distributions. *Quaternary Science Reviews* **232** (2020).

17. Schmittner, A. *et al.* Calibration of the carbon isotope composition (δ13C) of benthic foraminifera. *Paleoceanography* **32,** 512–530 (2017).

18. Mackensen, A. & Licari, L. in *The South Atlantic in the Late Quaternary* 623–644 (Springer, 2003).

19. Lear, C. H. *et al.* Breathing more deeply: Deep ocean carbon storage during the mid-Pleistocene climate transition. *Geology* **44,** 1035–1038 (2016).

20. Howe, J. N. & Piotrowski, A. M. Atlantic deep water provenance decoupled from atmospheric CO\textsubscript{2} concentration during the lukewarm interglacials. *Nature Communications* **8,** 2003 (2017).

21. Merino, N. *et al.* Antarctic icebergs melt over the Southern Ocean : Climatology and impact on sea ice. *Ocean Modelling* **104,** 99–110 (2016).

22. Keany, J., Ledbetter, M., Watkins, N. & Huang, T. C. Diachronous deposition of ice-rafted debris in sub-Antarctic deep-sea sediments. *Bulletin of the Geological Society of America* **87,** 873–882 (1976).

23. Diekmann, B. *et al.* in *The South Atlantic in the Late Quaternary* 375–399 (Springer, 2003).

24. Weber, M. E. *et al.* Millennial-scale variability in Antarctic ice-sheet discharge during the last deglaciation. *Nature* **510,** 134–138 (2014).

25. Teitler, L. *et al.* Determination of Antarctic Ice Sheet stability over the last ˜500 ka through a study of iceberg-rafted debris. *Paleoceanography* **25,** 1–18 (2010).

26. Gersonde, R., Crosta, X., Abelmann, A. & Armand, L. Sea-surface temperature and sea ice distribution of the Southern Ocean at the EPILOG Last Glacial Maximum - A circum-Antarctic view based on siliceous microfossil records. *Quaternary Science Reviews* **24,** 869–896 (2005).

27. Wolff, E. W. *et al.* Southern Ocean sea-ice extent, productivity and iron flux over the past eight glacial cycles. *Nature* **440,** 491–496 (2006).

28. Wagner, T. J. *et al.* Wave inhibition by sea ice enables trans-Atlantic ice rafting of debris during Heinrich events. *Earth and Planetary Science Letters* **495,** 157–163 (2018).

29. Schodlok, M. P., Hellmer, H. H., Rohardt, G. & Fahrbach, E. Weddell Sea iceberg drift: Five years of observations. *Journal of Geophysical Research: Oceans* **111,** 1–14 (2006).

30. Tournadre, J., Bouhier, N., Girard-Ardhuin, F. & Rémy, F. Antarctic icebergs distributions 1992-2014. *Journal of Geophysical Research: Oceans* **121,** 327–349 (2016).

31. Teitler, L. *et al.* Antarctic Ice Sheet response to a long warm interval across Marine Isotope Stage 31: A cross-latitudinal study of iceberg-rafted debris. *Earth and Planetary Science Letters* **409,** 109–119 (2015).

32. Pollard, D. & DeConto, R. M. Modelling West Antarctic ice sheet growth and collapse through the past five million years. *Nature* **458,** 329–332 (2009).

33. Silva, T. A., Bigg, G. R. & Nicholls, K. W. Contribution of giant icebergs to the Southern Ocean freshwater flux. *Journal of Geophysical Research: Oceans* **111,** 1–8 (2006).

34. Sun, S., Eisenman, I. & Stewart, A. L. Does Southern Ocean Surface Forcing Shape the Global Ocean Overturning Circulation? *Geophysical Research Letters* **45,** 2413–2423 (2018).

35. Gordon, A. L. Interocean exchange of thermocline water. *Journal of Geophysical Research* **91,** 5037 (1986).

36. Scussolini, P., Marino, G., Brummer, G. J. A. & Peeters, F. J. Saline Indian Ocean waters invaded the South Atlantic thermocline during glacial termination II. *Geology* **43,** 139–142 (2015).

37. Seidov, D., Stouffer, R. J. & Haupt, B. J. Is there a simple bi-polar ocean seesaw? *Global and Planetary Change* **49,** 19–27 (2005).

38. Stouffer, R. J., Seidov, D. & Haupt, B. J. Climate response to external sources of freshwater: North Atlantic versus the Southern Ocean. *Journal of Climate* **20,** 436–448 (2007).

39. Schmittner, A. Southern Ocean sea ice and radiocarbon ages of glacial bottom waters. *Earth and Planetary Science Letters* **213,** 53–62 (2003).

40. Menviel, L. *et al.* Poorly ventilated deep ocean at the Last Glacial Maximum inferred from carbon isotopes: A data-model comparison study. *Paleoceanography* **32,** 2–17 (2017).

41. Molyneux, E. G., Hall, I. R., Zahn, R. & Diz, P. Deep water variability on the southern Agulhas Plateau: Interhemispheric links over the past 170 ka. *Paleoceanography* **22** (2007).

42. Imbrie, J. *et al.* On the Structure and Origin of Major Glaciation Cycles 1. Linear Responses to Milankovitch Forcing. *Paleoceanography* **7,** 701–738 (1992).

43. Brathauer, U. & Abelmann, A. Late quaternary variations in sea surface temperatures and their relationship to orbital forcing recorded in the Southern Ocean (Atlantic sector). *Paleoceanography* **14,** 135–148 (1999).

44. Venz, K. A., Hodell, D. A., Stanton, C. & Warnke, D. A. A 1.0 Myr record of Glacial North Atlantic Intermediate Water variability from ODP site 982 in the northeast Atlantic. *Paleoceanography* **14,** 42–52 (1999).

45. Timmermann, A. *et al.* Modeling obliquity and CO2 effects on southern hemisphere climate during the past 408 ka. *Journal of Climate* **27,** 1863–1875 (2014).

46. Romero, O. E. *et al.* High-latitude forcing of diatom productivity in the southern Agulhas Plateau during the past 350 kyr. *Paleoceanography* **30,** 118–132 (2015).

47. Willeit, M., Ganopolski, A., Calov, R. & Brovkin, V. Mid-Pleistocene transition in glacial cycles explained by declining CO2 and regolith removal. *Science Advances* **5,** 1–9 (2019).

48. Rodríguez-Sanz, L., Graham Mortyn, P., Martínez-Garcia, A., Rosell-Melé, A. & Hall, I. R. Glacial Southern Ocean freshening at the onset of the Middle Pleistocene Climate Transition. *Earth and Planetary Science Letters* **345-348,** 194–202 (2012).

49. Raymo, M. E., Lisiecki, L. E. & Nisancioglu, K. H. Plio-pleistocene ice volume, antarctic climate, and the global δ18O record. *Science* **313,** 492–495 (2006).

50. Pena, L. D. & Goldstein, S. L. Thermohaline circulation crisis and impacts during the mid-Pleistocene transition. *Science* **345,** 318–322 (2014).

Figure Captions

Figure 1: Modelled iceberg trajectories and meridionally-averaged SST and meltwater distribution for the PI and LGM Atlantic Southern Ocean. **a.** Iceberg trajectories simulated by Pyberg for Pre-Industrial (PI) and Last Glacial Maximum (LGM) conditions (see online methods). Winter sea ice extent from[26] (15% concentration contour for September) is shown for PI and LGM. Surface ocean circulation is modified from[3]; AR = Agulhas Retroflection, AL = Agulhas Leakage, ARC = Agulhas Return Current. The shaded

grey band represents the Subtropical Frontal Zone (STFZ)[51]. **b.** 0-50°E zonal mean of mean SST under PI (pink) and LGM (blue) conditions. SST proxy data are from MARGO[26] (blue symbols; triangle = diatom, circle = radiolarian, square = alkenone). Model SST data are from COSMOS experiments (see online methods). The estimated meltwater distribution is given as total meltwater input in the 0-50°E zone as simulated by Pyberg (online methods), with values for the PI (pink) and LGM (blue) being the percentage of the total initial iceberg mass (added as icebergs in the yellow 'seeding region') which melts in the region.

Figure 2: Paleoceanographic proxy records from Mid- to Late-Pleistocene AP_{comp}. **a.** Time-series of $\delta^{13}C_{benthic}$ (top; pink, note reversed scale), IRD_{MAR} (middle; teal), and $\delta^{18}O_{benthic}$ (lower; grey, note reversed scale) from the AP_{comp} for the past 1.65 Ma, with glacial Marine Isotope Stages shaded grey. The interval 0-800 ka is expanded in panel **b.** which additionally includes the $Na_{sea\text{-}salt}$ accumulation from the EPICA Dome C Antarctic ice core[27], a proxy for SO sea-ice extent (top, purple). The AP_{comp} $U^{k'}_{37}$ SST record from[46] is also shown (second from top, orange). Note the log-scale for IRD_{MAR} in **b.**

Figure 3: IRD_{MAR} vs $\delta^{13}C_{benthic}$ lead-lag relationship. **a.** Blackman-Tukey coherency phase of IRD_{MAR} against $\delta^{13}C_{benthic}$ (red; triangular-head arrows) and $\delta^{18}O_{benthic}$ (blue; diamond-head arrows) in the 100 kyr^{-1}, 40 kyr^{-1}, and 23 kyr^{-1} frequency bands. These phase wheels are cropped at 0-90°, with clockwise rotation indicating a larger lead for IRD_{MAR} (given in kyrs on the curved axes). The arrow length represents coherency and the shaded areas give the 95% uncertainty in phase. IRD_{MAR} leads $\delta^{13}C_{benthic}$ and $\delta^{18}O_{benthic}$ in phase for all 3 frequencies. **b.** Summary of lead times for IRD_{MAR} over $\delta^{13}C_{benthic}$ determined by three independent approaches, with estimates of 95% uncertainty given by the back bars (see online methods).

Figure 4: The evolution of the AP_{MAR} IRD_{MAR} record in the time and frequency domain orbital forcing, global climate, and interhemispheric phasing. **a.** Results from the 'glacial accumulation' analysis: IRD_{MAR} and $\delta^{18}O_{benthic}$ time series are divided into glacial intervals, then the cummulative integral is taken within each interval and normalized to 100% in time and value. Glacial Progress % refers to the relative time between the onset and termination of each glacial interval. Accumulation refers to the normalized cumulative integral, for example 50% indicates that half of the total IRD_{MAR} deposited in that cycle has been deposited; if this falls to the right of the $\delta^{18}O_{benthic}$ curve, it suggests that IRD_{MAR} is accumulating relatively early within the glacial (see online methods). The three panels show the average and 95% bootstrap confidence intervals (s.e.m) for three periods: Marine Isotope Stage 1 (MIS 1) to MIS 10 (left), MIS 11 to MIS 36 (middle), and MIS 37 to MIS 59 (right). **b.** IRD_{MAR} on a log-scale (black) with orbital eccentricity (red, dashed line) and orbital obliquity (blue, dashed line) from[52]. Shaded grey bars (top) highlight glacial MISs and the blue gradient bar (second from top) indicate periods with dominant obliquity pacing.**c.** Wavelet analysis (using a Mortlet wave with zero-padding) of IRD_{MAR}, revealing the temporal evolution of relative power in the eccentricity (red-orange lines) and obliquity (blue lines) frequency bands. **d.** Inter-hemispheric comparison between the AP_{comp} IRD_{MAR} record (green; top) and a 1 Ma record of IRD (% IRD relative to planktonic foraminifera) from the North Atlantic site ODP 982[44] (bottom; grey; note reversed y-axis).

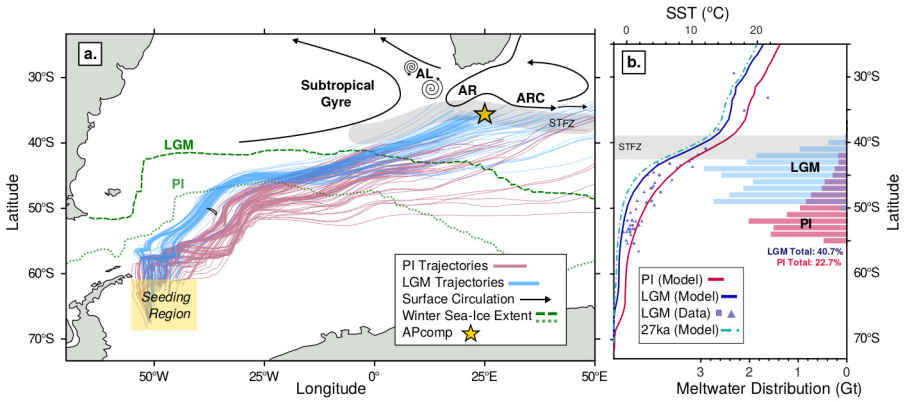

Figure 1:

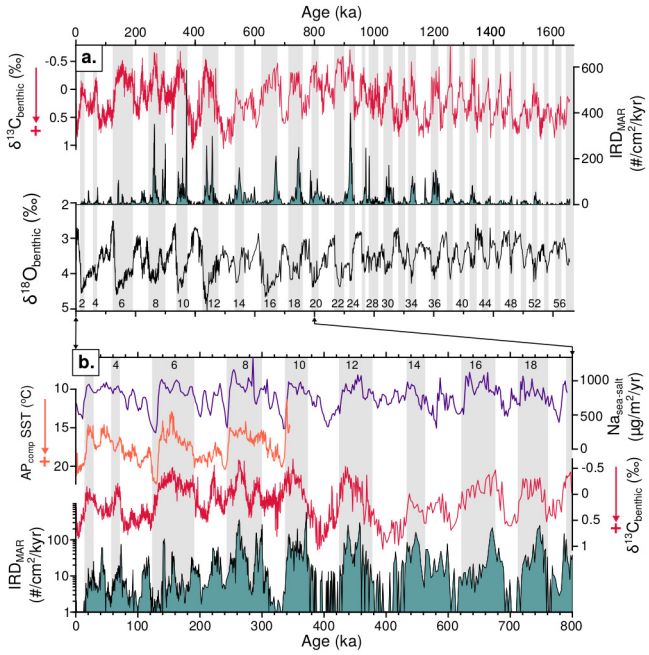

Figure 2:

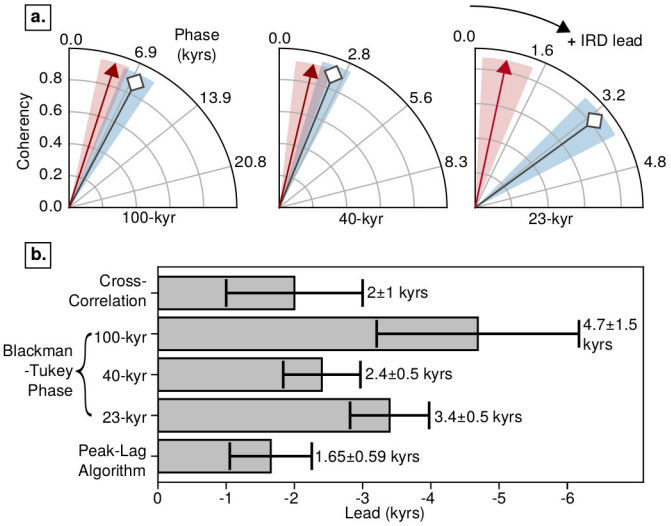

Figure 3:

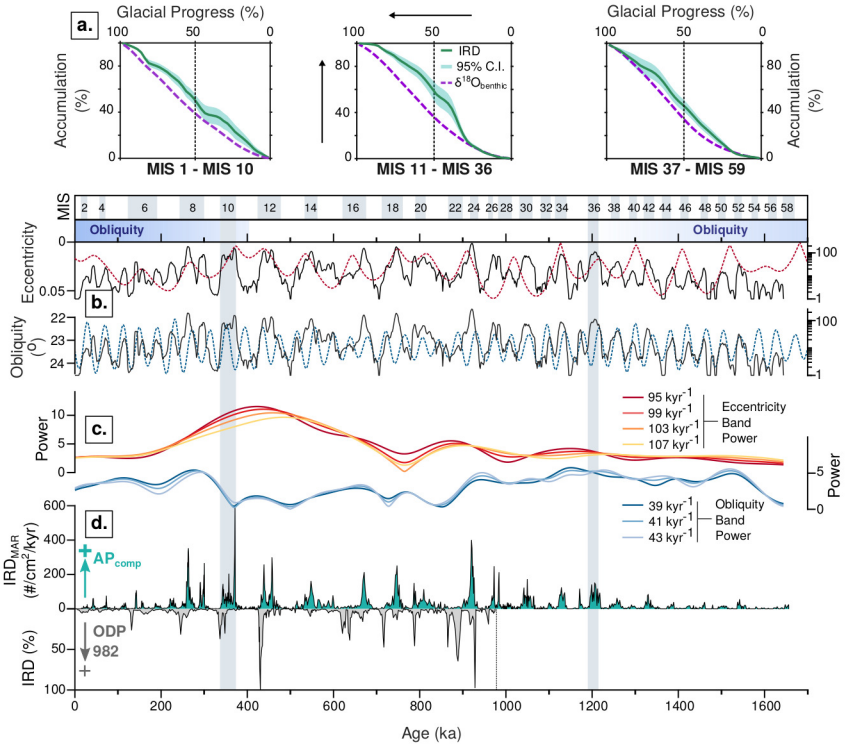

Figure 4:

Methods

AP_{comp}

The Agulhas Plateau composite (AP_{comp}) is a stratigraphic framework consisting of proximal sediment core sites MD02-2588 (41°19.90'S, 25°49.7'E, 2907m) and IODP Site U1475 (41°25.6'S, 25°15.6'E, 2669m). We utilise existing records from the upper 10.27m of MD02-2588 ($\delta^{18}O_{benthic}$ and $\delta^{13}C_{benthic}$ from[13], IRD counts from[11]) and correlated the lowest deglaciation in MD02-2588 to the respective deglaciation in Site U1475 using $\delta^{18}O_{benthic}$ and $\delta^{13}C_{benthic}$ from both cores. This tie point is at 10.27m in MD02-2588 and 8.16m on the U1475 Splice Extended Data Figure 2a). The chronology is based on graphically aligning $\delta^{18}O_{benthic}$ to the 'Prob-stack' (a probabilistic stack of $\delta^{18}O_{benthic}$ using a profile hidden Markov model;[53]). The Prob-stack includes 180 globally distributed $\delta^{18}O_{benthic}$ records and provides an update of the LR04 stack and timescale[54]. The Prob-stack and LR04 are similar over the MPT interval studied here. From selected age-depth markers (n = 45; consisting 12 radiocarbon dates and 33 $\delta^{18}O_{benthic}$ ties points; Extended Data Figure 2b), the final age-depth model was constructed using the deterministic age modelling routine Undatable[55] with 105 bootstrap simulations. The resultant sedimentation rates range from 1.2 cm/kyr to 7.6 cm/kyr, averaging 3.1 cm/kyr. The Brunhes/Matuyama magnetic reversal (0.781 Ma) and the Jaramillo Subchron (1.072 - 0.988 Ma) are identified in the U1475 down-core magnetic inclination[56], confirming the robustness of the final age-depth model. The records presented have a temporal resolution ranging from ~0.3 kyrs in the Late Pleistocene to ~1.5 kyrs in the early-mid Pleistocene. Stable isotope measurements were performed on 2-3 well-preserved Cibicidoides wuellerstorfi specimens (250-315μm size fraction) and made at Cardiff University using a Thermo Finnigan MAT 253 mass spectrometer linked online to a Carbo Kiel carbonate preparation device with long-term precision of ±0.05‰ for $\delta^{18}O$ and±0.021‰ for $\delta^{13}C$ ($\pm 1\sigma$). Results are calibrated to an internal laboratory standard (BCT63) and presented relative to the Vienna Pee Dee Belemnite scale.

Ice-Rafted Debris

IRD_{MAR} was determined by counting detrital mineral grains in the >150μm sediment fraction (subsampled using a micropaleontology splitter to yield 500-1000 entities) before normalization to sample weight (IRD concentration in #g) and then multiplication by apparent bulk mass accumulation rate (Extended Data Figure 2c), derived from estimates of dry bulk density from[57] and linear sedimentation rate. The temporal evolution, spectral characteristics, and timing of peaks in the IRD record are largely unaffected by conversion from concentration to Mass Accumulation Rate (MAR). This methodology is equivalent to that employed for MD02-2588 (the measurements for which were previously published by[11,12] n = 522), however as no dry bulk density (DBD) data is available for MD02-2588, we estimate it by using a 2nd order polynomial fitted to DBD in the overlapping interval of Site U1475 ($r^2 = 0.57$):

No quantitative distinction is presented between mineralogies of phenocrysts present, however grains that were clearly of volcanic (e.g. tephra) or authigenic (e.g. pyrite) were excluded from the IRD counts. Energy Dispersive X-Ray Spectrometry (EDS) point analysis was used to identify the mineralogy of several grains from a selection of samples (total grains = 31). Of the 31 measured, 23 were quartz (mostly 'clean' quartz with some Fe-K and Fe members), 7 were orthoclase (K-feldspar), and 1 was garnet (Almandine member) (Extended Data Figure 3). The origin of ice-rafted minerals in the Atlantic SO has been the topic of some discussion, as the presence of sea-ice rafted volcanic and mafic material in sediment cores close to volcanic Subantarctic islands can complicate the interpretation of IRD records[58,59]. However, the observed AP_{comp} assemblage of predominantly quartz with some K-feldspar and garnet is distinct from the plagioclase-dominated clear mineral assemblages found close to Bouvet Island[25,59]. This mineralogy implies a continental Antarctic origin[60]: the high quartz proportion may suggest a Ronne Ice Shelf,

Filchner Ice Shelf, or Antarctic Peninsula origin[60] whilst the presence of garnet indicates an East Antarctic contribution[25,60]. Micro-textures such as striations and step-like fractures identified on selected quartz grains further support a glacial origin[61].

Climate Model Experiments

We use a comprehensive fully coupled atmosphere–ocean general circulation model (AOGCM), COSMOS (ECHAM5-JSBACH-MPI-OM) in this study. The atmospheric model ECHAM5[62] complemented by the land surface component JSBACH[63], is used at T31 resolution (3.75°), with 19 vertical layers. The ocean model MPI-OM[64], including sea-ice dynamics that is formulated using viscous-plastic rheology[65], has a resolution of GR30 (3°×1.8°) in the horizontal, with 40 uneven vertical layers. The climate model has already been used to investigate a range of paleoclimate phenomena[15,66,67]. This indicates that it can capture key features of warm and cold climate and is thus a very suitable climate model for this study, especially glacial SO conditions and AABW formation[15]. In this study, to investigate responses of Antarctic iceberg transport to different climate backgrounds of the Southern Ocean, we utilized published equilibrium experiments under Pre-industrial (PI) and Last Glacial Maximum (LGM) boundary conditions[15]. To further assess roles of a lower-than-LGM obliquity (i.e. additional cooling on the glacial Southern Ocean), we further conducted one LGM sensitivity experiment with 27ka obliquity (22.25°) that is lower than the LGM value (22.949°). The three experiments are integrated to quasi-equilibrium and the average of the last 100 years is calculated to represent the corresponding climatology and used for modelling iceberg trajectory. The simulated climatological SO conditions of these runs can be found in Extended Data Figure 6.

Iceberg Trajectory Model

We use Pyberg (https://github.com/trackow/pyberg), an offline Python implementation of the FESOM-IB iceberg drift and decay module[14]. The model simulates iceberg trajectories and alongtrack rates of melting using established iceberg physics[68–70]. Pyberg reads monthly forcing data from different climates as simulated by the COSMOS climate model (10m winds and ocean currents for atmospheric and oceanic drags, sea surface height for the surface slope term, sea surface temperature for melting parameterizations). Monthly sea ice fields are also read and allow to lock icebergs into the sea ice when ice concentrations exceed 86%[29,70]. In that case, icebergs are advected along with the sea ice velocity field. Erosion of icebergs by surface waves is damped at high ice concentrations[69]. Pyberg uses the constant density roll-over criterion (Eq. 3 in[71]), which can be viewed as a more physical version of the widely adopted original ref.[72] formulation. Iceberg fracture is not included as parametrization of this process for climate models is still an active area of research[73,74].

Icebergs are initialized between 63°W-50°W in the iceberg alley of the Weddell Sea from an observationally-derived modern distribution of near-coastal iceberg positions and horizontal sizes (from[75]). The initial iceberg height is set to 250 m and the density to 850 kg/m3[33,75,76]. The total initial iceberg mass in the iceberg alley is thus 49.59 Gt. For consistency, and to start the icebergs within the ocean model domain, the initial positions are shifted 10°to the East for all experiments to account for the larger spatial extent of the Antarctic Ice Sheet during the last glacial maximum. Along-track melt-rates are gridded and summed on a 1°x1°regular grid to produce the meltwater distribution. The modelled PI trajectories are consistent with modern observational datasets[29,30] (Extended Data 7). The LGM results are broadly consistent with the previously published results from the Fine ResolUtion Greenland And Labrador (FRUGAL) intermediate complexity climate model iceberg module[16], with an equatorward shift and lengthening of trajectories in the Atlantic-Indian Southern Ocean Sector, however discrepancies are apparent such as the more extreme equatorward spread of LGM trajectories in the FRUGAL model compared to Pyberg.

This is the result of different iceberg seeding configurations (i.e. we introduce icebergs only in the 'iceberg alley' region and neglect possible Subantarctic sources) and variations in the forcing provided by the underlying climate models. We note that our interpretations based on the Pyberg results are entirely compatible with the results from FRUGAL, and the results of the latter suggest that our estimated meltwater redistribution is likely conservative. Furthermore, the Pyberg LGM results are supported by available ice-rafted debris records from the SO[22–25,77,78], which typically show a latitudinal divide between higher (lower) IRD accumulation at close to (away from) Antarctica during glacial compared to interglacial intervals.

Water-Mass Mixing Model

To identify the water mass signal on the AP_{comp} $\delta^{13}C_{benthic}$, we apply a simple binary mixing model (following[79]) to estimate the % of NSW from stacked $\delta^{13}C_{benthic}$ records representing NSW and SSW over the past 1.5 Ma:

$$\%NSW = 100x\frac{(\delta^{13}C_{AP}\text{comp} - \delta^{13}C_{SSW}}{\delta^{13}C_{NSW} - \delta^{13}C_{SSW}})$$

Where $\delta^{13}C_{NSW}$ is a shallow North Atlantic stack (consisting of ODP Sites 980, 982, 983;[80] and references therein) and $\delta^{13}C_{SSW}$ is a deep South Atlantic stack (consisting of ODP Sites 1089 and 1090;[81]). Stacks were created by converting all data onto the LR04[54] timescale, smoothing with a 5-kyr gaussian filter, and averaging. We apply this technique using both a SSW stack and a PDW stack as the second end-member, as in reality the "Southern" deep water-mass present in the glacial Atlantic is likely some combination of the two. For example, whilst several studies employ a PDW end-member[79,82,83], Raymo et al.[82] note that this is due to the absence of suitable Southern Ocean end-member records. Indeed, Venz and Hodell[84] later apply the same approach with newly available deep Southern Ocean $\delta^{13}C_{benthic}$ records. However, recent evidence indicates that PDW was present in the glacial Atlantic Ocean in larger proportions than previously thought[85] and so a PDW end-member may be preferable after all.

Times Series Analysis

The lagged cross-correlation between IRD_{MAR} against $\delta^{18}O_{benthic}$ and $\delta^{13}C_{benthic}$ is determined using the Gaussian-kernel-based cross-correlation algorithm of[86] (Extended Data figure 5b). This allows cross-correlation analysis to be performed on the original, irregularly-spaced data, in order to avoid the possibility of spurious phasing introduced by linear interpolation.

The 'peak-lag' algorithm we design to iteratively measure the offset between peaks in the rate of change of IRD_{MAR} and $\delta^{13}C_{benthic}$ is modified from the approach of[87] and analogous to 'Event Synchronisation' techniques. It smooths the time series, finds the first difference, and then measures the offset in local maxima of both signals. We tested the sensitivity of the algorithm to the smoothing filter selection, finding that the average lag computed for a range of filter designs (moving-average and Savitsky-Golay filters; orders between 1 and 21) give similar results within 1σ of each other. We additionally test the confidence that the result from our final chosen parameters (7-point moving-average) is significantly non-zero by performing 1000 'Monte Carlo' simulations with zero-lag red noise surrogates (generated from an autoregressive model of the real data), finding that the lag identified in our data (IRD_{MAR} vs $\delta^{13}C_{benthic}$) is significantly different from the surrogate series ($p<10^{-10}$); this additionally yields a 99% red noise confidence level of ±0.4 kyrs for the lag calculated for our data. We test the utility of the algorithm to detect lead-lag relationships in a series of surrogate time series with known lags applied by constructing synthetic time series from 3 sine waves (100, 41, 23-kyr periods), with higher-frequency oscillation (7-kyr period) and white-noise components added to emulate sub-orbital features. Known lags are imposed between pairs of the surrogate series. The results show that the algorithm performs well and is capable of detecting a lag of down to 0.4 kyrs to a confidence of $p<10^{-10}$. The algorithm shows an

inherent drift at higher lags (Extended Data figure 5a and b), meaning it underestimates lag times greater than 4 kyrs, however the 1.5 kyrs lag observed in our data should be short enough to be unaffected by this drift.

To divide the time series into glacial cycles (as in figure 4) we define intervals between peak interglacial conditions (identified as local minima in $\delta^{18}O_{benthic}$ separated by a minimum distance of 25-kyrs) and the next time $\delta^{18}O_{benthic}$ crosses an 'interglacial threshold' of 3.32‰(C. wuellerstorfi scale, equivalent to 3.75‰on the LR04-scale), which is lower than adopted by[88], but ensures that we do not define the interstadial MIS 5c as an interglacial. We manually add a peak interglacial marker at 506 ka (based on Northern Hemisphere perihelion) to include the 'cool' interglacial MIS 13a. Within each interval we calculate the cumulative integral of IRD_{MAR} and $\delta^{18}O_{benthic}$, before normalizing the values to percentages of total 'accumulation' for that interval (Extended Data figure 5d).

Finally, for the phase wheels in figure 3, we use the Blackman-Tukey method with a Bartlett window (using the Analyseries software[89]) after linearly interpolating (dt=1.5 kyrs) and standardizing (mean = 0, standard deviation = 1) the data.

Orbital Forcing and the Mid-Pleistocene Transition

We estimate the time-frequency spectral power in the AP_{comp} IRD_{MAR} time series by applying a continuous wavelet transform (using zero-padding and a Mortlet mother wave)[90]. To visualize the results, we extract the power (in units of normalized variance) at the 'Fourier periods' between 39 to 43 kyr^{-1} to represent frequencies associated with obliquity, and 92 to 108 kyr^{-1} to represent frequencies associated with eccentricity (figure 4c). We emphasise that this gives an estimate of relative not absolute spectral power in these bands. Between 1600 and ~900 ka, obliquity-band power is dominant, decreasing after 900 ka in favour of the ~100 kyr^{-1} power. This transition then reverses after ~400 ka, when obliquity-band power again dominates. It is important to note that spectral power at frequencies of ~40 kyr^{-1} and ~100 kyr^{-1} is not evidence for a direct forcing by the obliquity and eccentricity of Earth's orbit (with dominant periodicities at these values, respectively). Furthermore, it is instructive to also evaluate the timing of cycles in the IRD_{MAR} data relative to cycles in orbital parameters. In figure 4b-c, we show that while the spectral power is dominated by ~40 kyr^{-1} frequencies (pre- and post-MPT) there is a close coupling between high IRD_{MAR} and low obliquity. A mechanistic relationship here is supported by our climate model results (Extended Data 6) which indicate that the low obliquity 27ka experiment yields cooler SO SST and increased sea-ice extent relative to LGM. Indeed, a relationship between obliquity and SO seaice[15,91], as well as stronger westerlies (related to the increased latitudinal insolation gradient[45,92]) has been previously demonstrated; both would act to increase iceberg survivability and transport into and across the SAZ (Extended Data 7). However, the transient emergence of ~100 kyr^{-1} power between ~1.2 Ma and ~0.4 Ma coincides with the concealment of this apparent obliquity pacing. Recent modelling results have shown that SO sea ice is more sensitive to obliquity than its Northern Hemisphere counterpart[92], and one explanation for the obscuration could be a shift to more complex, non-linear pacing of SO climate as NH ice sheets expand and glacial-interglacial variations in atmospheric CO_2 increase[47]. The post-MBE return to obliquity-pacing might then indicate a shift in the nature of NH ice sheet growth, for example higher rate of growth relating to an increase in the Atlantic Inflow(SB, GK, XZ, et al., *submitted*).

Code Availability

Code for all data analysis presented is available at https://github.com/AidanStarr/Starr_et_al_2020 and code for the Pyberg model is available at https://github.com/trackow/pyberg.

Data Availability

All newly presented data will be available at doi.pangaea.de/10.1594/PANGAEA.921111 following acceptance.

Extended Data Figure Captions

Extended Data Figure 1: Schematic representation of the 'Southern Escape' mechanism described in this study. a. Shows an idealized representation of the Southern Ocean during Interglacial conditions. The front panel gives meridional-averaged overturning circulation (following[93]), with circulation divided into an Upper Cell and Lower Cell. Arrow width represents the relative strength of each circulation cell (wider being stronger). The top panel represents the ocean surface, with icebergs calving from the Antarctic Ice Sheet (AIS) and following a northward then eastward trajectory. The blue shading represents iceberg meltwater being entrained into the Lower Cell as icebergs melt south of the main Antarctic Circumpolar Current (ACC) belt. Orange wavy arrows represent brine rejection from sea-ice formation. The peach-coloured band represents the Subtropical Frontal Zone (STFZ) delineating the Subtropical regime to the north and the (sub)Antarctic regime to the South. **b.** Same as a., but for conditions during Glacial Inception; i.e. the transition from interglacial to glacial conditions. The major change from a. is the northward displacement of iceberg trajectories, resulting in much of the meltwater spreading northwards and being entrained in the Upper Cell, instead of Lower Cell. Secondly, colder surface conditions facilitate extended sea-ice cover, and subsequent increase in brine rejection. The Lower Cell thus experiences less positive buoyancy forcing from the combination of less iceberg meltwater and more brine rejection, becomes stronger. The Southern Escape of meltwater into the Upper Cell has not yet occurred in high enough amounts to perturb the Upper Cell and hence the geometries of the overturning cells are unchanged from a. **c.** Same as a. and b., but for full glacial conditions (occurring after b.). Here, the Southern Escape of meltwater has successfully perturbed the Upper Cell, which is now weaker and has contracted upwards. The now-dominant Lower Cell has thus increased in volume.

Extended Data Figure 2: AP_{comp} Age model and composite record construction. a. The appending of U1475 to the bottom of MD02-2588 using $\delta^{18}O_{benthic}$ with the new AP_{comp} composite depth scale on the right-hand axis. **b.** Age-depth tie points (circles) with the median and 95% confidence bounds for the deterministic age model. Depth is given on the AP_{comp} scale. **c.** The $\delta^{18}O_{benthic}$ from this study (purple) and the tuning target, the global delo stack[53] (light grey), and the implied linear sedimentation rates (black; dashed line) and calculated mass accumulation rate (green; solid line) from the final age model in the lower subplot.

Extended Data Figure 3: SEM Imaging and Mineralogy of IRD Grains from the AP_{comp}. a. An SEM image of a quartz grain from Site U1475 with an enlarged view of surface microtextures in the inset panel. **b-d.** SEM images of IRD grains with examples of relative peak intensities for elements derived from EDS point analyses. **b** shows a spectrum typical of quartz, **c** of garnet (almandine member), and **d** of K-feldspar (orthoclase). Scale bars are given in white on all SEM images.

Extended Data Figure 4: Comparison of $\delta^{13}C_{benthic}$ and water mass 'end-members'. a. Authigenic ϵNd isotope record from the deep equatorial Atlantic (ODP Site 154-929 from[20]; top, green), Smoothed $\delta^{13}C_{benthic}$ stacks for Northern-Sourced Water (NSW), Pacific Deep Water (PDW) and Southern-Sourced Water (SSW) end-members (see Methods for stack construction and constituent core sites) and the AP_{comp} $\delta^{13}C_{benthic}$ record. Selected Marine Isotope Stages (MIS) are shown as grey vertical shading. The bottom time series in **a.** shows % NSW at the AP_{comp} calculated using a binary mixing model with NSW

and a PDW (grey) or SSW (purple) end-members. **b.** Scatter plots of AP_{comp} $\delta^{13}C_{benthic}$ vs. %NSW calculated with an SSW (left) and PDW (middle) end-member, and vs. the ϵNd isotope record of[20] (right). Pearson's correlation coefficient r^2 is given. **c.** Shows Pre-Industrial $\delta^{13}C$ of Dissolved Organic Carbon (from[94] along a North-South (blue) and then East-West (red) transect, with the AP_{comp} position shown as a white circle.

Extended Data Figure 5: Time Series Analysis Algorithm Tests. a. and b. Testing the peak-lag algorithm to detect relationships in a series of surrogate time-series with known lags applied. The 'actual lag' axes represent the known lag-time imposed between pairs of the surrogate series and the 'calculated lag' axes show the lag estimated by the algorithm. A perfect performance would manifest as a 1:1 straight line through the scatter points. The violin plots in **b.** show the mean, median and kernel probability density estimates of calculated lags from 10^4 iterations of the test. **c.** Results of the 'glacial accumulation' algorithm with each shaded curve representing IRD_{MAR} (green) and $\delta^{18}O_{benthic}$ (purple) integrated and normalized to 100% within each glacial cycle. Above, the $\delta^{18}O_{benthic}$ record is shown (purple, solid) with green triangles denoting the peak interglacials identified and the dashed black line showing the $\delta^{18}O_{benthic}$ threshold above which the transitions from glacial to interglacial conditions are defined. **d.** Gaussian-kernel-based cross-correlation (gXCF, following[86]) function for AP_{comp} IRD_{MAR} vs. $\delta^{18}O_{benthic}$ and $\delta^{13}C_{benthic}$. The horizontal lines show the 95% Monte Carlo confidence levels for significant cross-correlation.

Extended Data Figure 6: COSMOS model experiment results. a-c. Annual mean sea surface height (SSH; shaded) in experiments (**a.** PI,**b.** LGM, **c.** 27ka). Solid/dashed contours represent 90%/15% sea ice concentration. **d-f.** As for **a-c.** but for climatological annual mean Sea Surface Temperature (SST). **g.** Anomaly of mean annual SSH between 27ka and LGM experiments. Solid/dashed contours give 90%/15% sea ice concentration (black and white lines represent LGM and 27ka, respectively). **h.** Same as **g.** but for SST.

Extended Data 7: Pyberg model experiment results. Pyberg results. **a., c., and e.** Spatial distribution of meltwater input estimated for 1 x 1°cells by Pyberg when forced by COSMOS outputs for Pre-Industrial (a; PI), Last Glacial Maximum (c; LGM), and Last Glacial Maximum 27ka (e; LGM27ka) conditions.In purple are observed modern iceberg trajectories from the BYU Giant Iceberg database[95] (QSCAT); the modelled PI trajectories appear substantially longer than the observed likely because icebergs are tracked in Pyberg even after then become too small to be identified and hence tracked by modern observational techniques. **b., d., and f.** Zonally averaged meltwater estimates for PI (b), LGM (d), and LGM27ka (f) experiments. The average is taken for each latitude between 0 and 50 °E; in other words, this shows the latitudinal distribution of meltwater across the Indian-Atlantic Ocean Gateway.

References

51. Graham, R. M. & De Boer, A. M. The Dynamical Subtropical Front. *Journal of Geophysical Research: Oceans* **118,** 5676–5685 (2013).

52. Laskar, J. *et al.* A long-term numerical solution for the insolation quantities of the Earth. *Astronomy & Astrophysics* **428,** 261–285 (2004).

53. Ahn, S., Khider, D., Lisiecki, L. E. & Lawrence, C. E. A probabilistic Pliocene–Pleistocene stack of benthic δ18O using a profile hidden Markov model. *Dynamics and Statistics of the Climate System* **2,** 1–16 (2017).

54. Lisiecki, L. E. & Raymo, M. E. A Pliocene-Pleistocene stack of 57 globally distributed benthic δ 18O records. *Paleoceanography* **20,** 1–17 (2005).

55. Lougheed, B. C. & Obrochta, S. P. A Rapid, Deterministic Age-Depth Modeling Routine for Geological Sequences With Inherent Depth Uncertainty. *Paleoceanography and Paleoclimatology* **34,** 122–133 (2019).

56. Hall, I. *et al.* in *Proceedings of the International Ocean Discovery Program, 361* (International Ocean Discovery Program, College Station, TX, 2017).

57. Gruetzner, J. *et al.* A New Seismic Stratigraphy in the Indian-Atlantic Ocean Gateway Resembles Major Paleo-Oceanographic Changes of the Last 7 Ma. *Geochemistry, Geophysics, Geosystems* **20,** 339–358 (2019).

58. Kanfoush, S. L. *et al.* Millennial-Scale Instability of the Antarctic Ice Sheet During the Last Glaciation. *Science* **288,** 1815–1819 (2000).

59. Nielsen, S. H., Hodell, D. A., Kamenov, G., Guilderson, T. & Perfit, M. R. Origin and significance of ice-rafted detritus in the Atlantic sector of the Southern Ocean. *Geochemistry, Geophysics, Geosystems* **8** (2007).

60. Diekmann, B. & Kuhn, G. Provenance and dispersal of glacial-marine surface sediments in the Weddell Sea and adjoining areas, Antarctica: Ice-rafting versus current transport. *Marine Geology* **158,** 209–231 (1999).

61. St John, K., Passchier, S., Tantillo, B., Darby, D. & Kearns, L. Microfeatures of modern sea-ice-rafted sediment and implications for paleo-sea-ice reconstructions. *Annals of Glaciology* **56,** 83–93 (2015).

62. Roeckner, E. *et al.* The atmospheric general circulation model ECHAM 5. PART I: Model description. Report / MPI für Meteorologie. http://hdl.handle.net/11858/00-001M-0000-0012-0144-5. *Report / Max-Planck-Institut für Meteorologie,* 349 (2003).

63. Brovkin, V., Raddatz, T., Reick, C. H., Claussen, M. & Gayler, V. Global biogeophysical interactions between forest and climate. *Geophysical Research Letters* **36,** 1–5 (2009).

64. Marsland, S. J., Haak, H., Jungclaus, J. H., Latif, M. & Röske, F. The Max-Planck-Institute global ocean/sea ice model with orthogonal curvilinear coordinates. *Ocean Modelling* **5,** 91–127 (2002).

65. Hibler, W. D. A Dynamic Thermodynamic Sea Ice Model. *Journal of Physical Oceanography* **9,** 815–846 (1979).

66. Wei, W. & Lohmann, G. Simulated atlantic multidecadal oscillation during the holocene. *Journal of Climate* **25,** 6989–7002 (2012).

67. Stärz, M., Jokat, W., Knorr, G. & Lohmann, G. Threshold in North Atlantic-Arctic Ocean circulation controlled by the subsidence of the Greenland-Scotland Ridge. *Nature Communications* **8,** 1–13 (2017).

68. Bigg, G. R., Wadley, M. R., Stevens, D. P. & Johnson, J. A. Modelling the dynamics and thermodynamics of icebergs. *Cold Regions Science and Technology* **26,** 113–135 (1997).

69. Gladstone, R. M., Bigg, G. R. & Nicholls, K. W. Iceberg trajectory modeling and meltwater injection in the Southern Ocean. *Journal of Geophysical Research: Oceans* **106,** 19903–19915 (2001).

70. Lichey, C. & Hellmer H., H. H. Modeling giant-iceberg drift under the influence of sea ice in the Weddell Sea, Antarctica. *Journal of Glaciology* **47,** 452–460 (2001).

71. Wagner, T. J., Stern, A. A., Dell, R. W. & Eisenman, I. On the representation of capsizing in iceberg models. *Ocean Modelling* **117,** 88–96 (2017).

72. Weeks, W. F. & Mellor, M. *Some Elements of Iceberg Technology.* **78-2,** 45–98 (Iowa State University Research Foundation, 1978).

73. Bouhier, N., Tournadre, J., Rémy, F. & Gourves-Cousin, R. Melting and fragmentation laws from the evolution of two large Southern Ocean icebergs estimated from satellite data. *Cryosphere* **12,** 2267–2285 (2018).

74. Wagner, T. J. *et al.* The "footloose" mechanism: Iceberg decay from hydrostatic stresses. *Geophysical Research Letters* **41,** 5522–5529 (2014).

75. Wesche, C. & Dierking, W. Near-coastal circum-Antarctic iceberg size distributions determined from Synthetic Aperture Radar images. *Remote Sensing of Environment* **156,** 561–569 (2015).

76. Barbat, M. M., Rackow, T., Hellmer, H. H., Wesche, C. & Mata, M. M. Three Years of Near-Coastal Antarctic Iceberg Distribution From a Machine Learning Approach Applied to SAR Imagery. *Journal of Geophysical Research: Oceans* **124,** 6658–6672 (2019).

77. Cooke, D. W. & Hays, J. D. Estimates of Antarctic Ocean seasonal sea-ice cover during glacial intervals. *Antarctic geoscience. 3rd symposium on Antarctic geology and geophysics, Madison, August 1977,* 1017–1025 (1982).

78. Grobe, H. & Mackensen, A. Late Quaternary climatic cycles as recorded in sediments from the Antarctic continental margin. *Antarctic Research Series - American Geophysical Union* **56,** 349–376 (1992).

79. Oppo, D. W. & Fairbanks, R. G. Variability in the deep and intermediate water circulation of the Atlantic Ocean during the past 25,000 years: Northern Hemisphere modulation of the Southern Ocean. *Earth and Planetary Science Letters* **86,** 1–15 (1987).

80. Raymo, M. E. *et al.* Stability of North Atlantic water masses in face of pronounced climate variability during the Pleistocene. *Paleoceanography* **19,** 1–13 (2004).

81. Hodell, D. *et al.* Data report: Oxygen isotope stratigraphy of ODP Leg 177 Sites 1088, 1089, 1090, 1093, and 1094. *Proceedings of the Ocean Drilling Program, 177 Scientific Results* **177** (2003).

82. Raymo, M. E., Oppo, D. W. & Curry, W. The mid-Pleistocene climate transition: A deep sea carbon isotopic perspective records from the deep ocean, extending back examined in order to constrain decrease in mean. *Paleoceanography* **12,** 546–559 (1997).

83. Lang, D. C. *et al.* Incursions of southern-sourced water into the deep North Atlantic during late Pliocene glacial intensification. *Nature Geoscience* **9,** 375–379 (2016).

84. Venz, K. A. & Hodell, D. A. New evidence for changes in Plio-Pleistocene deep water circulation from Southern Ocean ODP Leg 177 Site 1090. *Palaeogeography, Palaeoclimatology, Palaeoecology* **182,** 197–220 (2002).

85. Yu, J. *et al.* Last glacial atmospheric CO2 decline due to widespread Pacific deep-water expansion. *Nature Geoscience* **13,** 628–633 (2020).

86. Rehfeld, K., Marwan, N., Heitzig, J. & Kurths, J. Comparison of correlation analysis techniques for irregularly sampled time series. *Nonlinear Processes in Geophysics* **18,** 389–404 (2011).

87. Barker, S. *et al.* Icebergs not the trigger for North Atlantic cold events. *Nature* **520,** 333–336 (2015).

88. Berger, B. *et al.* Interglacials of the last 800,000 years. *Reviews of Geophysics* **54,** 162–219 (2016).

89. Paillard, D., Labeyrie, L. & Yiou, P. Macintosh Program performs time-series analysis. *Eos, Transactions American Geophysical Union* **77,** 379–379 (1996).

90. Grinsted, A., Moore, J. C. & Jevrejeva, S. Application of the cross wavelet transform and wavelet coherence to geophysical time series. *Nonlinear Processes in Geophysics* **11,** 561–566 (2004).

91. Fogwill, C. J., Turney, C. S., Hutchinson, D. K., Taschetto, A. S. & England, M. H. Obliquity control on Southern Hemisphere climate during the last glacial. *Scientific Reports* **5,** 1–10 (2015).

92. Wu, Z., Yin, Q., Guo, Z. & Berger, A. Hemisphere differences in response of sea surface temperature and sea ice to precession and obliquity. *Global and Planetary Change* **192,** 103223 (2020).

93. Marshall, J. & Speer, K. Closure of the meridional overturning circulation through Southern Ocean upwelling. *Nature Geoscience* **5,** 171–180 (2012).

94. Eide, M., Olsen, A., Ninnemann, U. S. & Johannessen, T. A global ocean climatology of preindustrial and modern ocean δ13C. *Global Biogeochemical Cycles* **31,** 515–534 (2017).

95. Budge, J. S. & Long, D. G. A Comprehensive Database for Antarctic Iceberg Tracking Using Scatterometer Data. *IEEE Journal of Selected Topics in Applied Earth Observations and Remote Sensing* **11,** 434–442 (2018).

End notes

Acknowledgements

This research used samples and/or data provided by the International Ocean Discovery Program (IODP). Funding for this research was provided by The Natural Environmental Research Council GW4+ Doctoral Training Partnership (AS) and NERC Grant NE/P000037/1 (IRH). AS acknowledges further funding through the Antarctic Science International Bursary. XZ acknowledges funding from Lanzhou University (Nr.225000-830006) and National Key R& D program of China (Nr.2018YFA0606403). FJJE acknowledges funding through Spanish Ministry of Science and Innovation (grant CTM2017-89711-C2-1-P), co-funded by the European Union through FEDER funds. L. Owen, S. Slater, A. Nedebragt and D. Muir are thanked for laboratory assistance.

Author Contributions

IODP Exp. 361 was led by IRH and SRH. All Exp. 361 Science Party contributed to sample collection. IRH formulated the research. AS performed laboratory analysis. AS performed data analysis with input from SB, IRH, GK, and HJLvdL. TR performed Pyberg experiments and XZ performed COSMOS experiments. AS wrote the manuscript with input from IRH, SB, GK, TR, XZ. All authors contributed to the interpretation of results and commented on the final manuscript.

Competing Interests

The authors declare no competing interests.

Corresponding Authors

Aidan Starr; StarrA1@Cardiff.ac.uk or Aidan.M.Starr@gmail.com Ian R. Hall; Hall@Cardiff.ac.uk

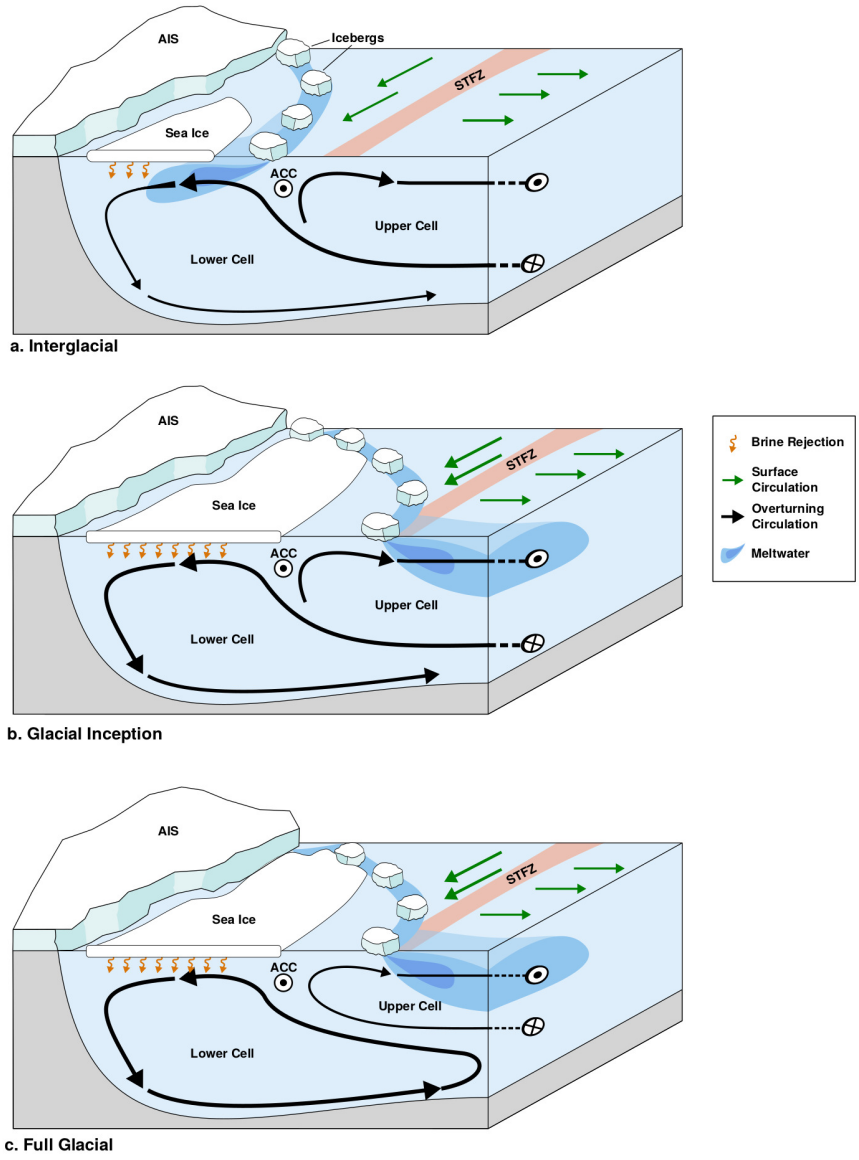

Extended Data Figure 1:

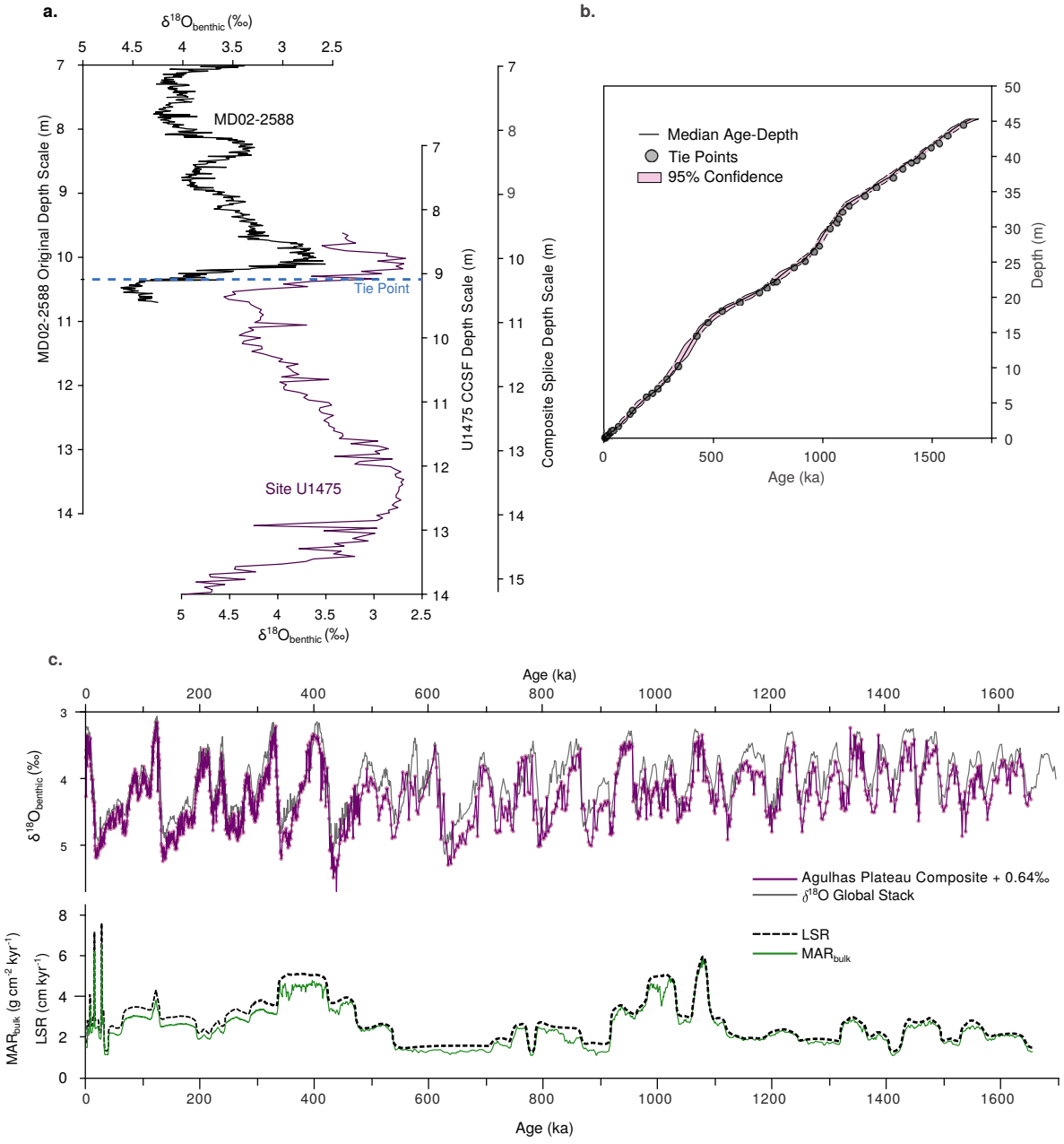

Extended Data Figure 2:

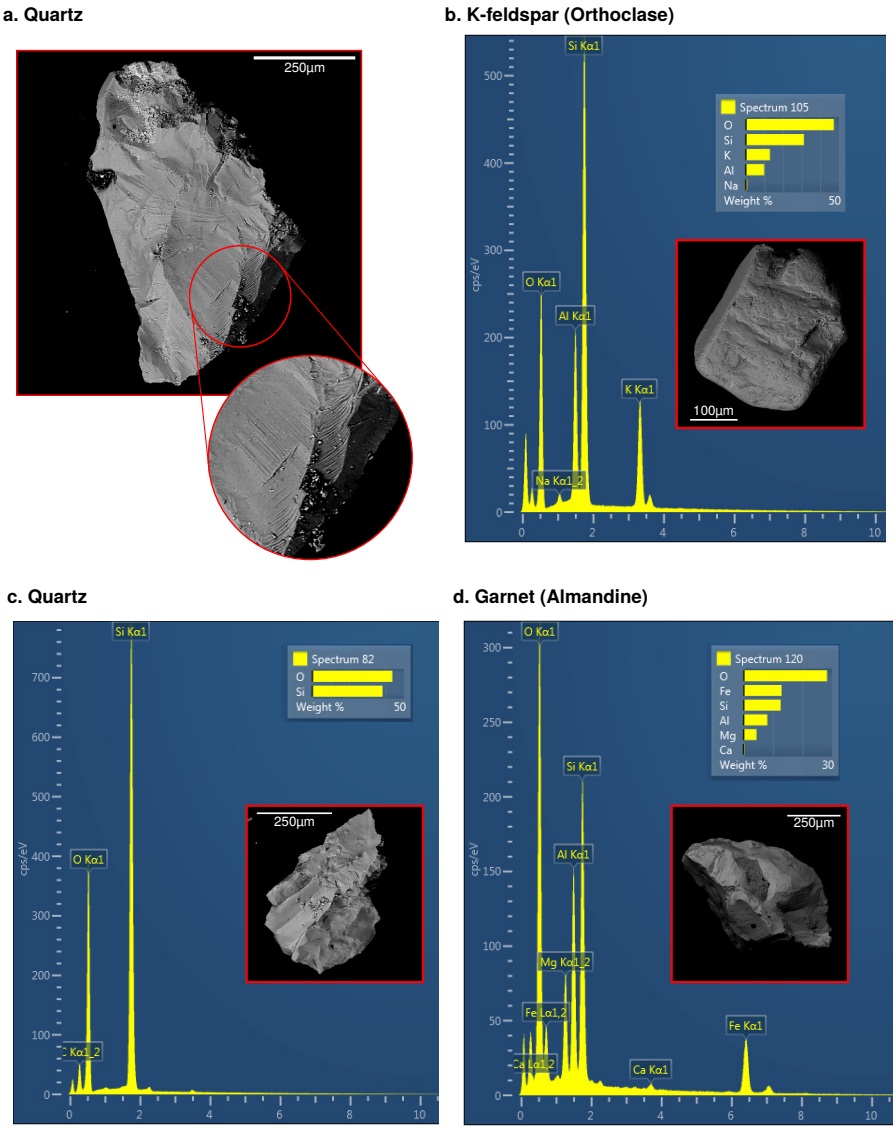

Extended Data Figure 3:

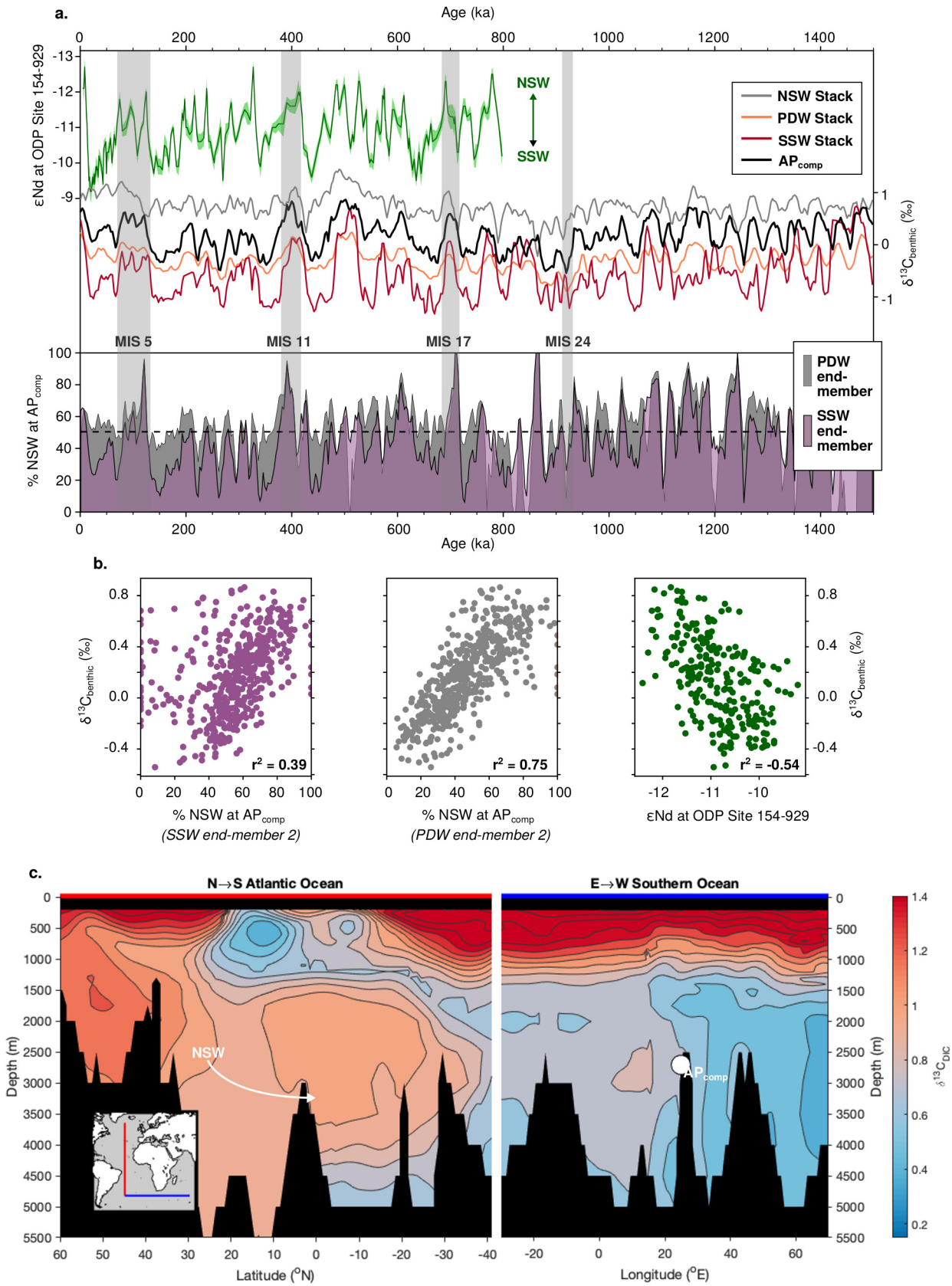

Extended Data Figure 4:

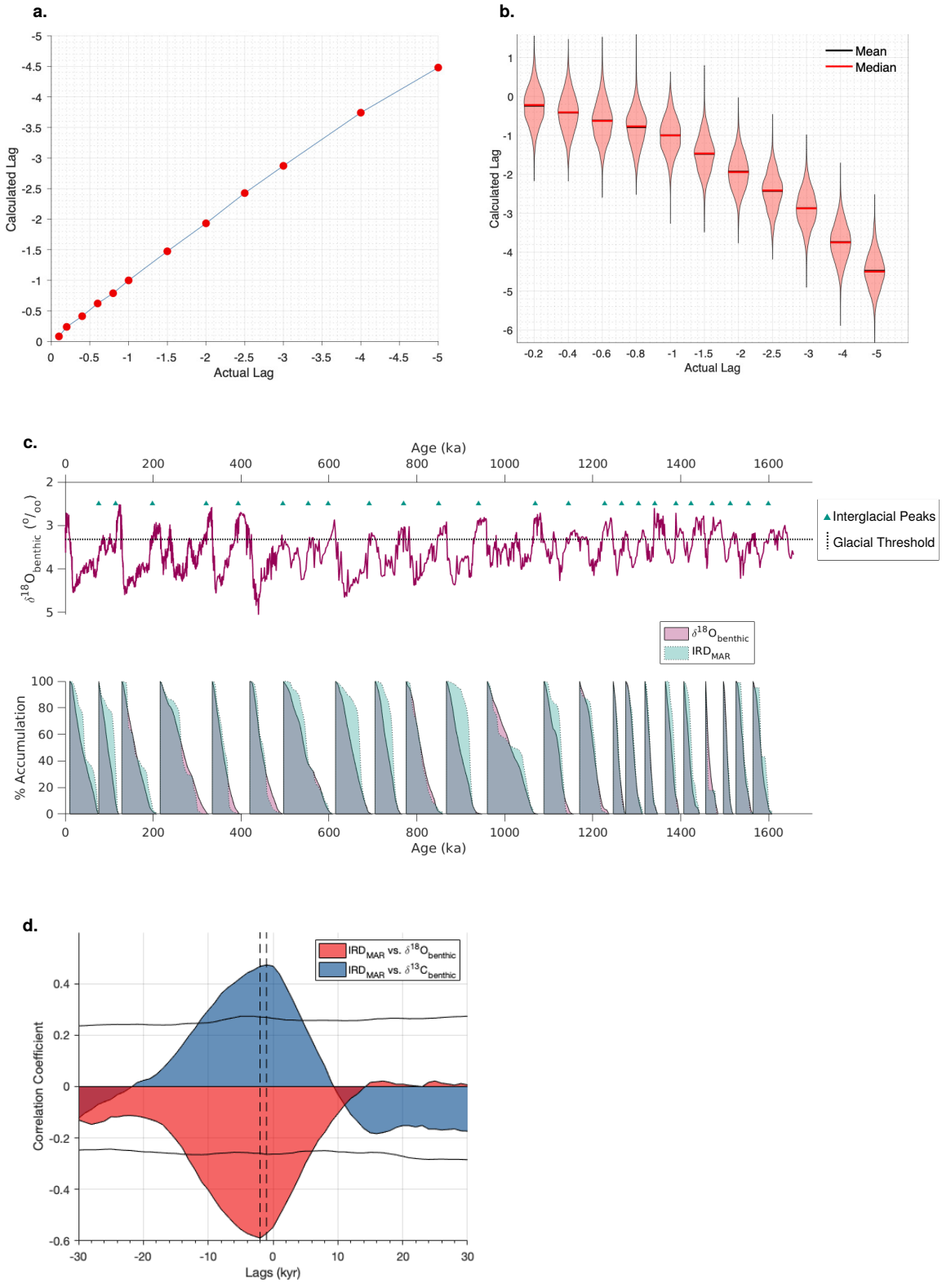

Extended Data Figure 5:

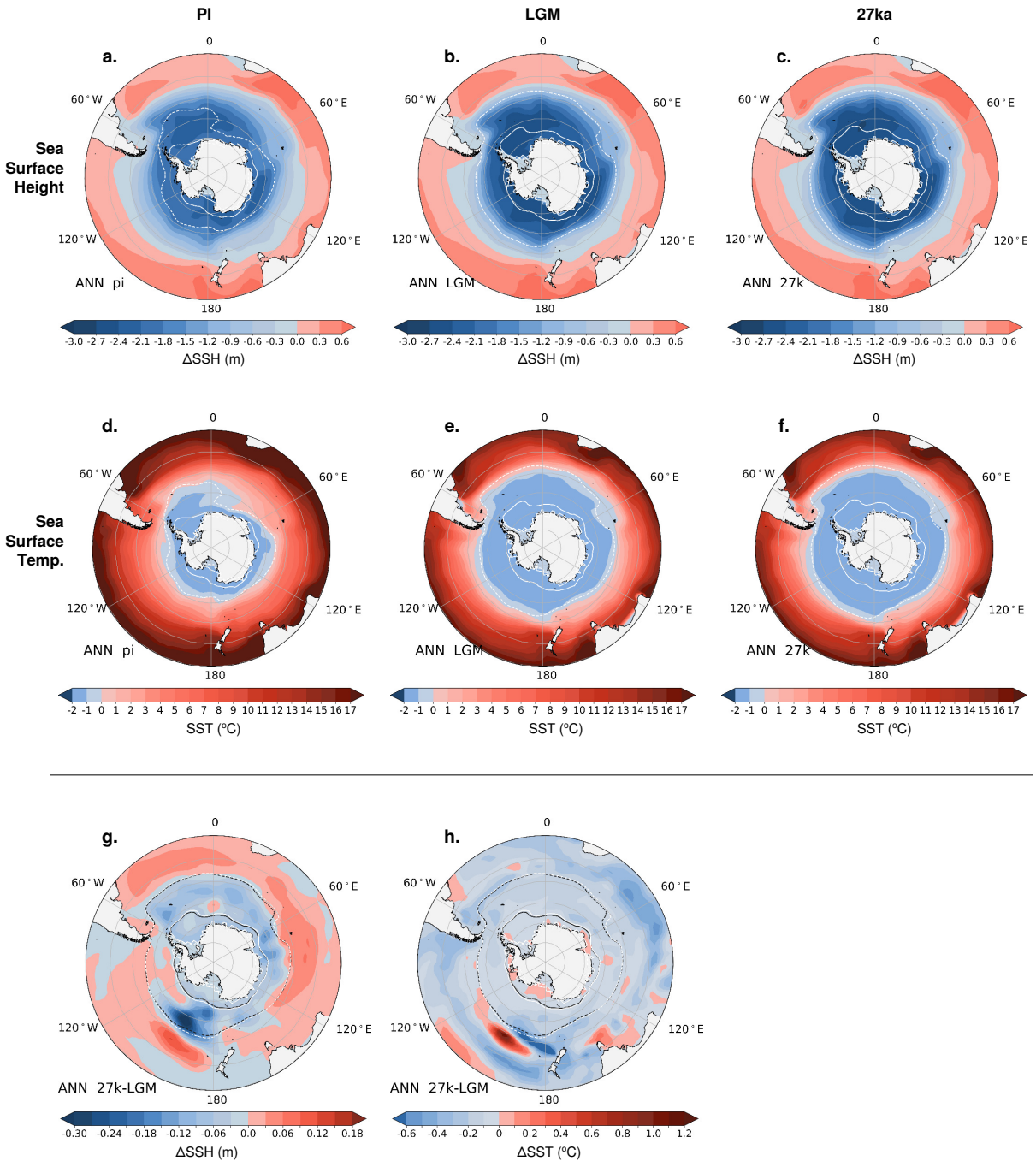

Extended Data Figure 6:

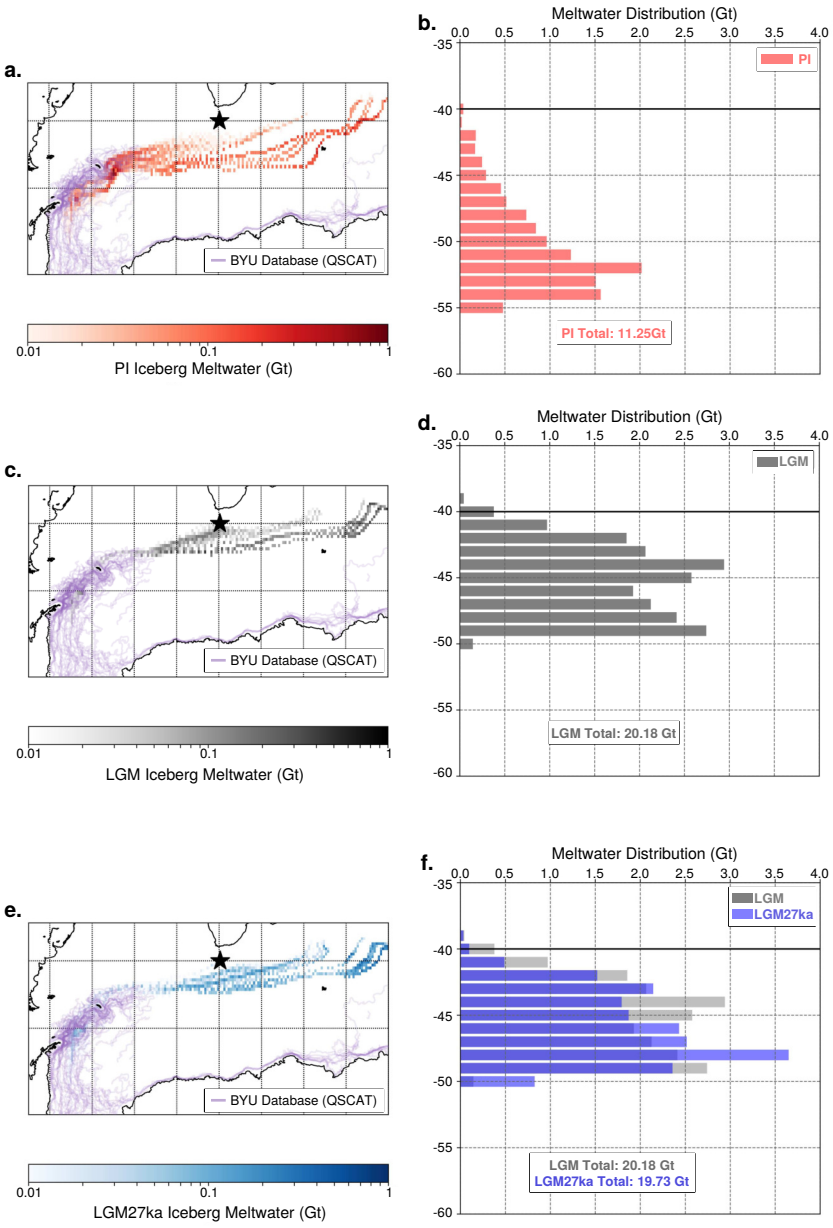

Extended Data Figure 7: